A&A 520, A13 (2010)
DOI: 10.1051/0004-6361/200913054

Astronomy & Astrophysics
Special feature

Pre-launch status of the Planck mission

Planck pre-launch status: High Frequency Instrument polarization calibration

C. Rosset[1,5], M. Tristram[1,11], N. Ponthieu[2], P. Ade[3], J. Aumont[2,11], A. Catalano[4,5], L. Conversi[16], F. Couchot[1], B. P. Crill[6,9], F.-X. Désert[7], K. Ganga[5], M. Giard[8], Y. Giraud-Héraud[5], J. Haïssinski[1], S. Henrot-Versillé[1], W. Holmes[9], W. C. Jones[6,9,14], J.-M. Lamarre[4], A. Lange[6,9†], C. Leroy[2,8], J. Macías-Pérez[7], B. Maffei[10], P. de Marcillac[2], M.-A. Miville-Deschênes[2], L. Montier[8], F. Noviello[2], F. Pajot[2], O. Perdereau[1], F. Piacentini[12], M. Piat[5], S. Plaszczynski[1], E. Pointecouteau[8], J.-L. Puget[2], I. Ristorcelli[8], G. Savini[3,15], R. Sudiwala[3], M. Veneziani[5,12], and D. Yvon[13]

[1] LAL, Laboratoire de l'Accélerateur Linéaire, CNRS Université Paris 11, Bâtiment 200, Orsay, France
e-mail: cyrille.rosset@apc.univ-paris-diderot.fr
[2] IAS, Institut d'Astrophysique Spatiale, CNRS Université Paris 11, Bâtiment 121, 91405 Orsay, France
[3] Astronomy and Instrumentation Group, Cardiff University, Cardiff, Wales, UK
[4] LERMA, CNRS, Observatoire de Paris, 61 Avenue de l'Observatoire, 75014 Paris, France
[5] APC, Astroparticule et Cosmologie, Université Paris Diderot, Bâtiment Condorcet, 10 rue Alice Domon et Léonie Duquet, 75205 Paris Cedex 13, France
[6] Observational Cosmology, California Institute of Technology, Mail code: 367-17, Pasadena, CA 91125, USA
[7] LAOG, Laboratoire d'Astrophysique Observatoire de Grenoble, CNRS, Grenoble, France
[8] CESR, CNRS, 9 Av. du colonel Roche, BP44346, 31038 Toulouse Cedex 4, France
[9] Jet Propulsion Laboratory, California Institute of Technology, Pasadena, CA 91109, USA
[10] The University of Manchester, JBCA, School of Physics and Astronomy, Manchester M13 9PL, UK
[11] LPSC, Laboratoire de Physique Subatomique et Cosmologie, CNRS, Grenoble, France
[12] Dipartimento di Fisica, Universitá di Roma "La Sapienza", 00185 Roma, Italy
[13] CEA, Service de Physique des Particules, Saclay, France
[14] Department of Physics, Princeton University, Princeton, NJ 08544, USA
[15] Optical Science Laboratory, University College London, Gower Street, WC1E 6BT London, UK
[16] European Space Astronomy Centre, PO Box 78, 28691 Villanueava de la Cañada (Madrid), Spain

Received 3 August 2009 / Accepted 7 April 2010

ABSTRACT

The High Frequency Instrument of *Planck* will map the entire sky in the millimeter and sub-millimeter domain from 100 to 857 GHz with unprecedented sensitivity to polarization ($\Delta P/T_{\rm cmb} \sim 4 \times 10^{-6}$ for P either Q or U and $T_{\rm cmb} \simeq 2.7$ K) at 100, 143, 217 and 353 GHz. It will lead to major improvements in our understanding of the cosmic microwave background anisotropies and polarized foreground signals. *Planck* will make high resolution measurements of the E-mode spectrum (up to $\ell \sim 1500$) and will also play a prominent role in the search for the faint imprint of primordial gravitational waves on the CMB polarization. This paper addresses the effects of calibration of both temperature (gain) and polarization (polarization efficiency and detector orientation) on polarization measurements. The specific requirements on the polarization parameters of the instrument are set and we report on their pre-flight measurement on HFI bolometers. We present a semi-analytical method that exactly accounts for the scanning strategy of the instrument as well as the combination of different detectors. We use this method to propagate errors through to the CMB angular power spectra in the particular case of *Planck*-HFI, and to derive constraints on polarization parameters. We show that in order to limit the systematic error to 10% of the cosmic variance of the E-mode power spectrum, uncertainties in gain, polarization efficiency and detector orientation must be below 0.15%, 0.3% and 1° respectively. Pre-launch ground measurements reported in this paper already fulfill these requirements.

Key words. space vehicles: instruments – techniques: polarimetric – instrumentation: polarimeters – instrumentation: detectors – cosmic microwave background – submillimeter: general

1. Introduction

The *Planck*[1] satellite, launched on May 14th, 2009, will map the whole sky in the range 30−857 GHz. One of the most exciting challenges for *Planck* is to measure the polarization anisotropies of the cosmic microwave background (CMB), which offers a unique way to constrain the energy scale of inflation.

CMB polarization can be decomposed into modes of even-parity (E-mode) and odd-parity (B-mode). Gravitational waves

[1] *Planck* (http://www.esa.int/Planck) is a project of the European Space Agency (ESA) with instruments provided by two scientific Consortia funded by ESA member states (in particular the lead countries: France and Italy) with contributions from NASA (USA), and telescope reflectors provided in a collaboration between ESA and a scientific Consortium led and funded by Denmark.

generated during inflation (hereafter "primordial" gravitational waves) create B-modes with a specific angular power spectrum, whose amplitude is related to the energy scale of inflation. A detection of these "primordial" B-modes would therefore provide the first measure of the energy scale of inflation.

E-modes were first detected by DASI in 2002, followed by other ground and balloon-borne experiments (Kovac et al. 2002; Readhead et al. 2004; Wu et al. 2007; Montroy et al. 2006; QUaD collaboration: Pryke et al. 2009) covering a few percent of the sky. These detections are complemented by the WMAP satellite observations of the whole sky (Page et al. 2007). All these measurements have confirmed the existence of an E-mode polarization compatible with the ΛCDM model, and are compatible with a B-mode polarization of zero. The tensor-to-scalar ratio r parametrizes the amplitude of B-mode polarization. The most stringent upper limit on r is obtained by Komatsu et al. (2009), combining WMAP measurements of TT, TE and EE power spectra with baryon acoustic oscillations and supernovae data. They obtain $r < 0.22$ if the scalar spectral index n_S is constant, or $r < 0.55$ if a running spectral index is allowed.

Planck has been designed to map the E-mode of polarization with high precision and good control over the polarization foreground contamination up to multipoles as large as $\ell \sim 1500$. *Planck* may also detect the B-mode polarization anisotropies, if tensor modes contribute at a level of a few percent or more of the amplitude of the scalar modes (Efstathiou & Gratton 2009). However, various instrumental systematic effects, induced by error on the knowledge of detector characteristics, may alter these measurements. Most of the properties of the detectors, such as the gain, time constant, bandpass and beam, are independent of the sensitivity to linear polarization. These properties are described in detail in companion papers (Pajot et al. 2010; Lamarre et al. 2010; Tauber et al. 2010a; Maffei et al. 2010). In this paper, we study the systematic effects induced by uncertainties in temperature and polarization calibration (gains, polarization efficiencies and orientations) on Stokes parameters and E and B-mode power spectra. We also report on the ground calibration of the polarization efficiencies and orientations of High Frequency Instrument (HFI) detectors. A study of polarization systematics for the Low Frequency Instrument (LFI) of *Planck* is presented in Leahy et al. (2010).

The paper is organized as follows. In Sect. 2, we present the polarization sensitive bolometers (PSBs) used by the *Planck*-HFI and the layout of the focal plane. Section 3 gives the generic expression of the polarized photometric equation and introduces the polarization-related systematic effects discussed in Sect. 4. In Sect. 5, we describe a semi-analytical method to propagate uncertainties on temperature and polarization calibration of detectors up to angular power spectra while exactly accounting for the scanning strategy and the combination of multiple detectors. We apply this method to the *Planck*-HFI in Sect. 6 and derive requirements on the knowledge of these parameters. Finally, Sect. 7 describes the procedure used to measure polarization parameters of the detectors on ground and compares them to the requirements derived in the previous section.

2. Detectors and focal plane layout

HFI uses bolometric detectors cooled to 100 mK to measure millimeter-wave radiation. They comprise a micro-mesh absorber in a form resembling a spider web to reduce cosmic ray interactions (hence the name spider-web bolometer or SWB, see Bock et al. 1995; Yun et al. 2004), heated by ohmic power dissipation, and a neutron transmutation doped (NTD) germanium thermistor that measures the temperature variation. Polarization is measured with specifically designed polarization sensitive bolometers (PSBs, see Jones et al. 2003), composed of a pair of bolometers that couple to orthogonal linear polarizations, allowing the measurement of I and (local) Q Stokes parameters (respectively the sum and difference of the signals of the two bolometers). The SWBs are only slightly sensitive to polarization, and PSBs do not perfectly reject the cross-polarization component. We define precisely the cross-polarization leakage in the next section. The HFI focal plane is composed of 20 SWBs and 16 PSB pairs, i.e., 32 polarization sensitive bolometers (see Fig. 1). The PSB pairs are grouped in pairs rotated by 45° and following the same track on the sky, with the angular separation between associated pairs ranging from 0.°5 to 2.°5. Thus, the difference signal within one pair measures Stokes Q (in some local reference frame) while the difference signal within the other pair measures Stokes U. Both pairs allow measurements of the total intensity through the sum of signals. This layout was chosen in order to minimize the noise on the Stokes parameters and their correlation (Couchot et al. 1999).

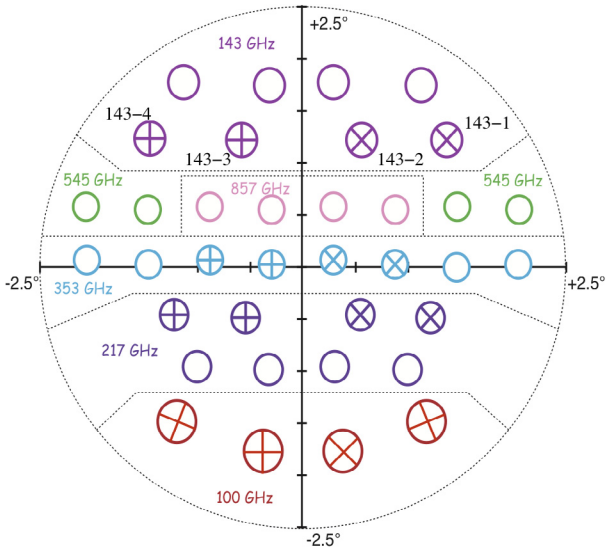

Fig. 1. Sky projection of the *Planck*-HFI focal plane. The crosses symbolize the polarization sensitive bolometers and indicate the orientation of the two linear polarization measured in each horn. The scanning direction is horizontal in this sketch, so that PSB pairs at same frequency follow the same track on the sky.

The satellite scans the sky by spinning at 1 rpm. The spin axis remains within 7.°5 of the anti-solar direction (for a detailed presentation of the *Planck* scanning strategy, see Tauber et al. 2010b). The angle between the spin axis and the line of sight is 85° ± 2.°5 depending on detector position in focal plane. The ecliptic pole regions are thus much more covered than the equatorial region, both in terms of number of hits per pixel and in different observation orientations. This means that around the ecliptic poles, each detector observes the sky with several focal plane orientations and hence measures I, Q and U. In contrast, in the equatorial region, at least three detectors must be combined to obtain the polarization signal. This is very different from currently designed ground or balloon-borne experiments in which the Stokes parameters can be measured using a single detector. This impacts the propagation of errors, as discussed in detail in Sect. 5.

3. Polarized photometric equation

In this section, we derive the expression for the power received by a PSB. Following Jones's notation (Jones 1941), the

polarization state of a plane wave can be described by its transverse electric field $\boldsymbol{e} = (E_x, E_y)$, where E_x and E_y are complex amplitudes. The transmission through an instrument can be described by its Jones matrix $\mathbf{J}_{\rm tot}$, a 2×2 complex matrix, which relates the radiation $\boldsymbol{e}_{\rm det}$ that hits a detector to the incoming radiation on the telescope $\boldsymbol{e}_{\rm sky}$:

$$\begin{aligned}\boldsymbol{e}_{\rm det}(\nu, \boldsymbol{n}) &= \mathbf{J}_{\rm tot}(\nu, \boldsymbol{n})\, \boldsymbol{e}_{\rm sky}(\nu, \boldsymbol{n}) \\ &= \mathbf{J}_{\rm det}\, \mathbf{J}_{\rm filter}(\nu)\, \mathbf{J}_{\rm beam}(\nu, \boldsymbol{n})\, \boldsymbol{e}_{\rm sky}\end{aligned} \quad (1)$$

where ν is the electromagnetic frequency, $\boldsymbol{n}$ is the direction of observation and we have decomposed the Jones matrix into optical element Jones matrices. As the detector is sensitive to polarization, we can write the associated Jones matrix $\mathbf{J}_{\rm det}$ as:

$$\mathbf{J}_{\rm det} = \begin{pmatrix} 1 & 0 \\ 0 & \sqrt{\eta} \end{pmatrix}, \quad (2)$$

where η is the cross-polarization leakage. We assume it is independent of the frequency of the incoming radiation, which is reasonable as it is mainly due to absorption of the cross-polarization component on the edge of the absorbing grid (Jones et al. 2003).

The filter can also be described by a Jones matrix, as it is not a depolarizing element in the sense defined by Ditchburn (1976). It is simply given by:

$$\mathbf{J}_{\rm filter} = \begin{pmatrix} \sqrt{\tau(\nu)} & 0 \\ 0 & \sqrt{\tau(\nu)} \end{pmatrix} \quad (3)$$

where $\tau(\nu)$ is the bandpass transmission of the filter, which has been measured accurately on ground.

Finally, the beam of both the telescope and the horns is described by a generic Jones matrix, $\mathbf{J}_{\rm beam}(\nu, \boldsymbol{n})$, which depends on both radiation frequency and direction on the sky. The electric field received by the detector is thus given by:

$$\boldsymbol{e}_{\rm det}(\nu, \boldsymbol{n}) = \sqrt{\tau(\nu)}\, \mathbf{R} \begin{pmatrix} J_{xx} & J_{xy} \\ \sqrt{\eta} J_{yx} & \sqrt{\eta} J_{yy} \end{pmatrix} \mathbf{R}^{-1} \boldsymbol{e}_{\rm sky}(\nu, \boldsymbol{n}) \quad (4)$$

where we have included the matrix $\mathbf{R}$ which rotates the incoming radiation from the sky reference frame to the intrument reference frame. The coefficients J_{ij}, with i, j in $\{x, y\}$, are the elements of the beam Jones matrix $\mathbf{J}_{\rm beam}(\nu, \boldsymbol{n})$.

The intensity measured by the detector is the sum of the intensities coming from each direction and for each frequency:

$$I_{\rm det} = \iint \langle \boldsymbol{e}_{\rm det}(\nu, \boldsymbol{n})^{\dagger} \cdot \boldsymbol{e}_{\rm det}(\nu, \boldsymbol{n}) \rangle \, {\rm d}\boldsymbol{n} \, {\rm d}\nu. \quad (5)$$

To describe the sky signal, we use the Stokes parameters I, Q, U and V (see, e.g., Born & Wolf 1964):

$$\begin{aligned} I(\nu, \boldsymbol{n}) &= \langle E_x E_x^* \rangle + \langle E_y E_y^* \rangle \\ Q(\nu, \boldsymbol{n}) &= \langle E_x E_x^* \rangle - \langle E_y E_y^* \rangle \\ U(\nu, \boldsymbol{n}) &= \langle E_x E_y^* \rangle + \langle E_y E_x^* \rangle \\ V(\nu, \boldsymbol{n}) &= -i \left(\langle E_x E_y^* \rangle - \langle E_y E_x^* \rangle \right), \end{aligned} \quad (6)$$

where I is the intensity, Q and U charaterize the linear polarization and V the circular polarization of the sky radiation. We define analogously the beam Stokes parameters as:

$$\begin{aligned} \tilde{I}_\alpha(\nu, \boldsymbol{n}) &= J_{\alpha x} J_{\alpha x}^* + J_{\alpha y} J_{\alpha y}^* \\ \tilde{Q}_\alpha(\nu, \boldsymbol{n}) &= J_{\alpha x} J_{\alpha x}^* - J_{\alpha y} J_{\alpha y}^* \\ \tilde{U}_\alpha(\nu, \boldsymbol{n}) &= J_{\alpha x} J_{\alpha y}^* + J_{\alpha y} J_{\alpha x}^* \\ \tilde{V}_\alpha(\nu, \boldsymbol{n}) &= -i \left(J_{\alpha x} J_{\alpha y}^* - J_{\alpha y} J_{\alpha x}^* \right) \end{aligned} \quad (7)$$

($\alpha = x, y$). Note that in general the beam Stokes parameters depend on both frequency and sky direction. Therefore, we can write the intensity measured by the detector as:

$$\begin{aligned} I_{\rm det} = \frac{1}{2} \iint \tau(\nu) \Big[& I(\tilde{I}_x + \eta \tilde{I}_y) \\ & + Q \left[(\tilde{Q}_x + \eta \tilde{Q}_y) \cos 2\theta - (\tilde{U}_x + \eta \tilde{U}_y) \sin 2\theta \right] \\ & + U \left[(\tilde{Q}_x + \eta \tilde{Q}_y) \sin 2\theta + (\tilde{U}_x + \eta \tilde{U}_y) \cos 2\theta \right] \\ & - V(\tilde{V}_x + \eta \tilde{V}_y) \Big] \end{aligned} \quad (8)$$

where θ is the angle of orientation between the sky and detector reference frames, and we have not explicitly written the dependency of radiation and beam Stokes parameters to frequency ν and direction $\boldsymbol{n}$ for clarity.

4. Systematics for polarization

In Eq. (8) each term that couples to one of the Stokes parameters may depend on the direction of observation, $\boldsymbol{n}$, and on frequency in non trivial ways. Several other instrumental effects could be added to give an accurate description of a detector measurement, such as its time constant, noise or pointing errors.

The final calibration and analysis of HFI data needs to address all these effects and will rely on both ground and in-flight measurements. This is beyond the scope of this paper. However, some comments can already be made.

HFI beam patterns have been simulated with GRASP (see Maffei et al. 2010; Tauber et al. 2010a) and these simulations have been verified by ground calibration performed by Thales Industries. It was shown that *optical* cross-polarization and circular polarization $\tilde{V}$ due to telescope were less than 0.1%. Their impact has been studied separately (Rosset et al. 2007).

We will thus consider in the following an ideal optical system for which $\mathbf{J}_{\rm beam}$ is proportional to the identity matrix resulting in $\tilde{I}_x = \tilde{I}_y = \tilde{Q}_x = -\tilde{Q}_y$ and $\tilde{U}_x = \tilde{U}_y = \tilde{V}_x = \tilde{V}_y = 0$. Equation (8) therefore simplifies to

$$I_{\rm det} = \frac{1}{2} \iint \tau(\nu) \tilde{I}_x [(1+\eta) I + (1-\eta)(Q \cos 2\theta + U \sin 2\theta)] \, {\rm d}\Omega {\rm d}\nu. \quad (9)$$

Realistic bandpasses and frequency dependence of optical beam coupling terms are non-trivial effects that affect absolute calibration. More specifically, calibration could depend on the electromagnetic spectrum of the source. This is expected to impact component separation. In this work, we focus on systematic effects on CMB polarization and rely on absolute calibration on the CMB dipole, the amplitude f which is known to 0.5% accuracy (Fixsen et al. 1994). We expect to measure in flight the relative gain to an accuracy of better than 0.2%, given the gain stability expected for HFI (i.e. better than WMAP, see Hinshaw et al. 2009). Beam asymmetries and pointing errors couple to the scanning strategy of the instrument. A general framework to assess their impact is presented in Shimon et al. (2008) and O'Dea et al. (2007).

Leaving these effects aside for this work, the measurement of a detector reads:

$$m = g \Big(I + \rho [Q \cos 2(\psi + \alpha) + U \sin 2(\psi + \alpha)] \Big) + n \quad (10)$$

in which n is the noise, g is the total *gain*, $\rho = (1 - \eta)/(1 + \eta)$ is commonly referred to as *polarization efficiency*, ψ is the dependence on the focal plane orientation on the sky and α stands for the relative *detector orientation* with respect to it.

5. Propagation of errors for polarization calibration

In this section, we propagate errors on gain g, on polarization efficiency ρ and detector orientation α (as defined in the previous section) up to Stokes parameters (Sect. 5.1) and angular power spectra (Sect. 5.2).

This method applies to all polarization experiments observing with total power detectors such as HFI bolometers. It is close to the approach taken by Shimon et al. (2008) and O'Dea et al. (2007). A similar approach, focused on coherent receivers, was first proposed by Hu et al. (2003). The main difference of the method presented here is that it addresses the specific case of *Planck* which combines different detectors to determine Q and U.

5.1. Error on Stokes parameters

Given a pixelization of the sky and gathering all samples that fall into the same pixel p in a vector $\boldsymbol{m}$, Eq. (10) generalizes to the usual matrix form:

$$m_t = A_{tp} s_p + n_t, \tag{11}$$

in which $\boldsymbol{s} = (I, Q, U)$ is the pixelized polarized sky signal and $\boldsymbol{n}$ represents the noise vector. The pointing matrix $\mathbf{A}$ encodes both the direction of observation and the photometric equation including the calibration parameters g, ρ and α. Projection of time-ordered data into a pixelized map is done by solving Eq. (11) for $\boldsymbol{s}$, knowing $\boldsymbol{m}$ and the noise covariance matrix $N \equiv \langle \boldsymbol{n}\boldsymbol{n}^T \rangle$. The maximum likelihood solution is $\widehat{\boldsymbol{s}} = (\mathbf{A}^T\mathbf{N}^{-1}\mathbf{A})^{-1}\mathbf{A}^T\mathbf{N}^{-1}\boldsymbol{m} = (\mathbf{A}^T\mathbf{A})^{-1}\mathbf{A}^T\boldsymbol{m}$ if we consider only Gaussian, white and piece wise stationary noise, as we shall do in the remaining part of this work in order to focus on systematic effects.

We use a perturbative approach of assumed parameters $\tilde{g}$, $\tilde{\rho}$ and $\tilde{\alpha}$ (leading to a pointing matrix $\tilde{\mathbf{A}}$) around their true values g, ρ and α (leading to $\mathbf{A}$). From Eq. (10), we can see that for Q and U Stokes parameters, errors on the gain and polarization efficiency are degenerate. In the following, we use an effective polarization efficiency $\rho' \equiv g\rho$ and keep g for intensity only. The actual gain, polarization efficiency and orientation for a given detector d are therefore $g_d = \tilde{g}_d + \gamma_d$, $\rho'_d = \tilde{\rho}_d{}' + \epsilon_d$ and $\alpha_d = \tilde{\alpha}_d + \omega_d$ respectively[2]. Thus, ignoring noise,

$$\hat{\boldsymbol{s}} = (\tilde{\mathbf{A}}^T\tilde{\mathbf{A}})^{-1}\tilde{\mathbf{A}}^T\boldsymbol{m} \tag{12}$$

$$= \left[\sum_d \tilde{\mathbf{A}}_d^T\tilde{\mathbf{A}}_d\right]^{-1}\left[\sum_d \tilde{\mathbf{A}}_d^T\mathbf{A}_d\right]\boldsymbol{s} \tag{13}$$

$$\equiv \left[\sum_d \tilde{\mathbf{A}}_d^T\tilde{\mathbf{A}}_d\right]^{-1}\left[\sum_d \mathbf{\Lambda}_d(\gamma_d, \epsilon_d, \omega_d)\right]\boldsymbol{s}. \tag{14}$$

In this expression, $\mathbf{\Lambda}_d(\gamma, \epsilon_d, \omega_d)$ is an explicit function of γ, ϵ_d and ω_d, and $\tilde{g}$, $\tilde{\rho}'$ and $\tilde{\alpha}$ are only parameters.

Considering small variations around g, ρ' and α, we can write the perturbative expansion to first order for both $\gamma \ll 1$, $\epsilon \ll 1$ and $\omega \ll 1$:

$$\Delta\boldsymbol{s} = \hat{\boldsymbol{s}} - \boldsymbol{s} = \left[\sum_d \tilde{\mathbf{A}}_d^T\tilde{\mathbf{A}}_d\right]^{-1}\left[\sum_d \mathbf{\Lambda}_d(\gamma_d, \epsilon_d, \omega_d) - \mathbf{\Lambda}_d(0,0,0)\right]\boldsymbol{s}$$

$$\simeq \left[\sum_d \tilde{\mathbf{A}}_d^T\tilde{\mathbf{A}}_d\right]^{-1}\sum_d\left[\frac{\partial\mathbf{\Lambda}_d}{\partial\gamma_d}\gamma_d + \frac{\partial\mathbf{\Lambda}_d}{\partial\epsilon_d}\epsilon_d + \frac{\partial\mathbf{\Lambda}_d}{\partial\omega_d}\omega_d\right]\boldsymbol{s}. \tag{15}$$

[2] In the following, when a relation holds for γ, ϵ or ω, we simply write e.

Partial derivatives with respect to gain γ_d, polarization efficiency ϵ_d and orientation ω_d uncertainties are derived in Appendix A.

The errors $\Delta\boldsymbol{s}$ strongly depend on the scanning strategy through the number of hits per pixel and the distribution of detector orientations. These are accounted for exactly by taking the scanning strategy of the instrument and the positions of all detectors, and computing the pointing-related quantities per pixel on which $\mathbf{\Lambda}_d$ and its derivatives depend. This part of the work may be intensive in terms of memory or disk access requirements depending on which experiment is being modeled but needs to be performed only once. Then, given a sky model, the generation of an arbitrary large set of error maps $\Delta\boldsymbol{s}$ requires fewer resources and involves only distributions of γ_d, ϵ_d and ω_d.

Note that in the particular case of an experiment whose scanning strategy is such that each detector observes each pixel of the map under angles uniformly distributed over $[0, \pi]$, making a combined map as in Eq. (12) is equivalent to making one set of I, Q, and U maps per detector and co-adding them to obtain the final optimal maps of the experiment. In that case, sums of cosines and sines vanish, which means that off diagonal terms of $\tilde{\mathbf{A}}_d^T\tilde{\mathbf{A}}_d$ are zero and Eq. (15) reads simply

$$\Delta\boldsymbol{s} = \langle\gamma\rangle_d\begin{pmatrix} I \\ 0 \\ 0 \end{pmatrix} + \langle\frac{\epsilon}{\rho'}\rangle_d\begin{pmatrix} 0 \\ Q \\ U \end{pmatrix} + 2\langle\omega\rangle_d\begin{pmatrix} 0 \\ U \\ -Q \end{pmatrix}. \tag{16}$$

Because of the linearization, the final map is sensitive to the averages of these parameters. If errors are correlated (or identical at worst), they do not average down; if they are randomly distributed around zero mean, they do. These results are in agreement with O'Dea et al. (2007). As we will see in the Sect. 6, this is not the case for HFI, for which none of these simplifications applies.

5.2. Errors on angular power spectra

Following conventions of Zaldarriaga & Seljak (1997), the projection onto spherical harmonics of intensity and polarization reads:

$$a^T_{\ell m} = \int I(\boldsymbol{n}) Y^*_{lm}(\boldsymbol{n})\, \mathrm{d}\boldsymbol{n},$$

$$a^E_{\ell m} = -\int \left[Q(\boldsymbol{n})R^+_{lm}(\boldsymbol{n}) + iU(\boldsymbol{n})R^-_{lm}(\boldsymbol{n})\right]\, \mathrm{d}\boldsymbol{n},$$

$$a^B_{\ell m} = i\int \left[Q(\boldsymbol{n})R^-_{\ell m}(\boldsymbol{n}) + iU(\boldsymbol{n})R^+_{lm}(\boldsymbol{n})\right]\, \mathrm{d}\boldsymbol{n}$$

where the $R^\pm_{lm} = {}_2Y^*_{lm} \pm {}_{-2}Y^*_{lm}$ depend on the s-spin spherical harmonic functions ${}_sY_{lm}(\boldsymbol{n})$ ($s = \{0, 2, -2\}$).

Spherical harmonics transforms are linear, so derivatives of $\boldsymbol{a}_{\ell m} = \left(a^T_{\ell m}, a^E_{\ell m}, a^B_{\ell m}\right)$ read

$$\frac{\partial\boldsymbol{a}_{\ell m}}{\partial e} = \int\begin{pmatrix} Y^*_{lm} & 0 & 0 \\ 0 & -R^+_{lm} & -iR^-_{lm} \\ 0 & iR^-_{lm} & -R^+_{\ell m} \end{pmatrix}_{(\boldsymbol{n})}\frac{\partial\boldsymbol{s}}{\partial e}(\boldsymbol{n})\, \mathrm{d}\boldsymbol{n}.$$

We use a simple pseudo-C_ℓ estimator, $\tilde{C}_\ell$, which is χ^2-distributed with a mean equal to the underlying C_ℓ, $\nu_\ell = (2\ell + 1)$ degrees of freedom and a variance of $2C_\ell/\nu_\ell$:

$$\tilde{C}^{XY}_\ell = \frac{1}{(2\ell+1)}\sum_{m=-\ell}^{\ell} a^{X*}_{\ell m}a^Y_{\ell m}. \tag{17}$$

This estimator neglects the $E-B$ mixing due to incomplete sky coverage (Lewis et al. 2002) and assumes a cross-power spectrum for which noise bias is null (or if auto-spectra are used, that the noise bias has been previously removed) because their interaction with the systematic effects introduced here are of second order.

Using the previous relations, straightforward algebra leads from Eq. (15) to its counterpart in harmonic space:

$$\Delta\tilde{C}_\ell = \sum_d \frac{\partial\tilde{C}_\ell}{\partial\gamma_d}\gamma_d + \sum_d \frac{\partial\tilde{C}_\ell}{\partial\epsilon_d}\epsilon_d + \sum_d \frac{\partial\tilde{C}_\ell}{\partial\omega_d}\omega_d + \frac{1}{2}\sum_{d,d'}\left[\frac{\partial^2\tilde{C}_\ell}{\partial\gamma_d\partial\gamma_{d'}}\gamma_d\gamma_{d'} + \frac{\partial^2\tilde{C}_\ell}{\partial\epsilon_d\partial\epsilon_{d'}}\epsilon_d\epsilon_{d'} + \frac{\partial^2\tilde{C}_\ell}{\partial\omega_d\partial\omega_{d'}}\omega_d\omega_{d'}\right], \tag{18}$$

where, for $e = \gamma$, ϵ or ω,

$$\frac{\partial C_\ell^{XY}}{\partial e} = \frac{1}{2\ell+1}\sum_{m=-\ell}^{\ell}\left[\frac{\partial a_{\ell m}^{X*}}{\partial e}a_{\ell m}^{Y} + a_{\ell m}^{X*}\frac{\partial a_{\ell m}^{Y}}{\partial e}\right] \tag{19}$$

$$\frac{\partial^2 C_\ell^{XY}}{\partial e\partial e'} = \frac{1}{2\ell+1}\sum_{m=-\ell}^{\ell}\left[\frac{\partial^2 a_{\ell m}^{X*}}{\partial e\partial e'}a_{\ell m}^{Y} + \frac{\partial a_{\ell m}^{X*}}{\partial e}\frac{\partial a_{\ell m}^{Y}}{\partial e'} + \frac{\partial a_{\ell m}^{X*}}{\partial e'}\frac{\partial a_{\ell m}^{Y}}{\partial e} + a_{\ell m}^{X*}\frac{\partial^2 a_{\ell m}^{Y}}{\partial e\partial e'}\right]. \tag{20}$$

We ignore cross-terms between different systematic parameters so the previous expressions are only applicable when all but one of the parameters are set to zero. The cross-terms have been checked to be one order of magnitude below the direct terms. Note that we push the perturbative expansion to second order, since E-modes are much larger than B-modes and a second order effect on E-modes has an impact comparable to a first order effect on B-modes.

5.3. Monte-Carlo simulations

We have now everything in hand to perform the semi-analytical estimate of the polarization calibration systematic effects. The method can be described in 5 main steps:

1. From the scanning strategy of the instrument, for each detector d, project into a map: $\cos 2\psi$, $\sin 2\psi$, $\cos 2\psi \sin 2\psi$, and $\cos^2 2\psi$.
2. With these quantities, compute for each pixel of the map the following 3×3 matrices: $\left[\sum_d \tilde{\mathbf{A}}_d^T\tilde{\mathbf{A}}_d\right]^{-1}$, $\mathbf{\Lambda}_d$, and its first and second derivatives.
3. Use a simulated CMB sky $\boldsymbol{s}$ and Eq. (15) to compute partial derivatives $\partial\boldsymbol{s}/\partial e$ (up to second order).
4. Compute all cross-power spectra between $\boldsymbol{s}$ and its derivatives.
5. Combine these results using gaussian random distributions of γ_d, ϵ_d and ω_d (with various rms σ) in Eq. (18) to obtain the final error on the angular power spectrum.

The power spectra estimator used is a pseudo-C_ℓ estimator based on the cross-power spectra algorithm (Tristram et al. 2005), extended to polarization (Kogut et al. 2003; Grain et al. 2009). The semi-analytic method described in this section has been compared to full Monte-Carlo simulations and gives results compatible with statistical expectations for the number of simulations performed.

6. Application to *Planck*-HFI focal plane

We apply the method described in the previous section to the *Planck*-HFI to set requirements on gain, polarization efficiency and orientation. We simulated HEALPix (Górski et al. 2005) full-sky maps at a resolution of ~3.5 arcmin ($nside = 1024$) so that all pixels are seen and each pixel is uniformly sampled. This avoids the complications of estimating power spectra on a cut sky when allowing for the same conclusions, as our power spectrum estimator is not biased in the mean. The scanning strategy that we use is a realistic simulation of what *Planck* will actually do in a 14-month mission. The sky signal is pure CMB simulated from the best ΛCDM fit to WMAP 5 years data (Dunkley et al. 2009) with $r = 0.05$, supposing the CMB signal to be dominant over foregrounds residuals (at least for intensity and E-mode CMB signals).

As described in Sect. 2, the *Planck* scanning strategy and focal plane design do not allow the data from a single PSB pair to provide independent maps of the Stokes parameters. Here, we will use two PSB pairs calibrated in intensity and consider small variations around their gain $g_d = 1$, nominal angles $\alpha_d = \{0°, 90°, 45°, 135°\}$ and nominal polarization efficiency $\rho'_d = 1$ (corresponding to perfect PSB).

6.1. Error on Stokes parameter for HFI

We refer to Appendix A for the explicit form of the derivative terms of the Stokes parameters. Here, we emphasize the issues specific to HFI. In this case, Eq. (15) reads (see Eqs. (A.9)–(A.14))

$$\Delta\boldsymbol{s} = \begin{pmatrix}\Delta_{II} & \Delta_{IQ} & \Delta_{IU}\\ \Delta_{QI} & \Delta_{QQ} & \Delta_{QU}\\ \Delta_{UI} & \Delta_{UQ} & \Delta_{UU}\end{pmatrix}\boldsymbol{s}. \tag{21}$$

For gain variations only, non-zero elements of the matrix are given for each pixel, to first order, by

$$\Delta_{II}^{g} = \frac{1}{4}(\gamma_1+\gamma_2+\gamma_3+\gamma_4) \tag{22}$$

$$\Delta_{QI}^{g} = \frac{1}{4}(\gamma_1-\gamma_2)\langle\cos 2\psi\rangle - \frac{1}{4}(\gamma_3-\gamma_4)\langle\sin 2\psi\rangle \tag{23}$$

$$\Delta_{UI}^{g} = \frac{1}{4}(\gamma_1-\gamma_2)\langle\sin 2\psi\rangle + \frac{1}{4}(\gamma_3-\gamma_4)\langle\cos 2\psi\rangle. \tag{24}$$

For polarization efficiency only, elements of the matrix are given for each pixel, to first order, by

$$\Delta_{IQ}^{\rho} = \frac{1}{4}(\epsilon_1-\epsilon_2)\langle\cos 2\psi\rangle - \frac{1}{4}(\epsilon_3-\epsilon_4)\langle\sin 2\psi\rangle \tag{25}$$

$$\Delta_{IU}^{\rho} = \frac{1}{4}(\epsilon_1-\epsilon_2)\langle\sin 2\psi\rangle + \frac{1}{4}(\epsilon_3-\epsilon_4)\langle\cos 2\psi\rangle \tag{26}$$

$$\Delta_{QQ}^{\rho} = \frac{1}{2}(\epsilon_1+\epsilon_2)\left\langle\cos^2 2\psi\right\rangle + \frac{1}{2}(\epsilon_3+\epsilon_4)\left\langle\sin^2 2\psi\right\rangle \tag{27}$$

$$\Delta_{QU}^{\rho} = \frac{1}{2}\left[(\epsilon_1+\epsilon_2)-(\epsilon_3+\epsilon_4)\right]\langle\cos 2\psi\sin 2\psi\rangle \tag{28}$$

$$\Delta_{UQ}^{\rho} = \frac{1}{2}\left[(\epsilon_1+\epsilon_2)-(\epsilon_3+\epsilon_4)\right]\langle\cos 2\psi\sin 2\psi\rangle \tag{29}$$

$$\Delta_{UU}^{\rho} = \frac{1}{2}(\epsilon_1+\epsilon_2)\left\langle\sin^2 2\psi\right\rangle + \frac{1}{2}(\epsilon_3+\epsilon_4)\left\langle\cos^2 2\psi\right\rangle. \tag{30}$$

In the case of orientation errors only, to first order,

$$\Delta^{\alpha}_{IQ} = -\frac{1}{2}(\omega_1 - \omega_2)\langle \sin 2\psi\rangle - \frac{1}{2}(\omega_3 - \omega_4)\langle \cos 2\psi\rangle \quad (31)$$

$$\Delta^{\alpha}_{IU} = \frac{1}{2}(\omega_1 - \omega_2)\langle \cos 2\psi\rangle - \frac{1}{2}(\omega_3 - \omega_4)\langle \sin 2\psi\rangle \quad (32)$$

$$\Delta^{\alpha}_{QQ} = -\left[(\omega_1 + \omega_2) - (\omega_3 + \omega_4)\right]\langle \cos 2\psi \sin 2\psi\rangle \quad (33)$$

$$\Delta^{\alpha}_{QU} = (\omega_1 + \omega_2)\left\langle \cos^2 2\psi\right\rangle + (\omega_3 + \omega_4)\left\langle \sin^2 2\psi\right\rangle \quad (34)$$

$$\Delta^{\alpha}_{UQ} = -(\omega_1 + \omega_2)\left\langle \sin^2 2\psi\right\rangle - (\omega_3 + \omega_4)\left\langle \cos^2 2\psi\right\rangle \quad (35)$$

$$\Delta^{\alpha}_{UU} = \left[(\omega_1 + \omega_2) - (\omega_3 + \omega_4)\right]\langle \cos 2\psi \sin 2\psi\rangle\,. \quad (36)$$

In these Eqs. (22)–(36), the average is over the samples falling into a given pixel. It depends only on the scanning strategy. Figure 2 shows the angle distribution on the sky for a realistic *Planck* scanning strategy. *Planck* shows large inhomogeneities that induce additional terms with respect to the case of a single bolometer.

Leakage from intensity to polarization. Error on gain only produces leakage from intensity to polarization (see Eq. (A.8)). This leakage is driven by the relative errors inside a given horn which indicates that an absolute error on the gain (same for all detectors) will not produce any leakage. Neither polarization efficiency nor detector orientation errors induce any leakage from I into polarization Q and U (see Eqs. (A.9)–(A.14)).

Leakage from polarization to intensity. Both polarization efficiency and orientation error produce leakage from polarization to intensity. It is driven by the difference of errors within one horn and the relative weight of each horn depends on the distribution of ψ (see Fig. 2).

Polarization mixing. Polarization calibration parameters mix both Q and U. This means that they induce leakage from Q to U through the term Δ^{ρ}_{QU} (and from U to Q through the term Δ^{ρ}_{UQ}) but also alter the amplitude of polarization (Δ^{ρ}_{QQ} and $\Delta^{\rho}_{UU} \neq 0$). If we consider identical errors for each detector, we are in the limiting case where orientation error induces only leakage (Eqs. (34), (35)) and polarization efficiency only changes the amplitude of polarization (Eqs. (27), (30)) as described by Eq. (16). In the case of *Planck*-HFI, and considering independent errors, none of these simplifications apply. In particular, different parameter averages from one horn to the other induce both Q and U mixing and amplitude modification.

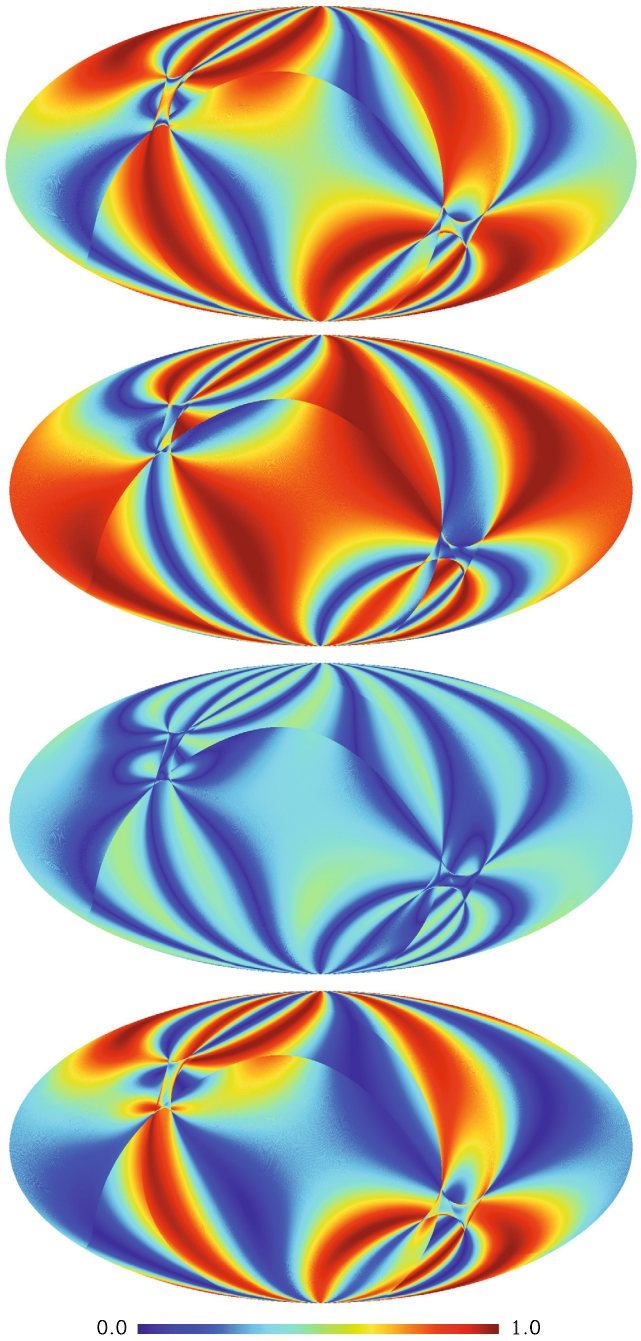

Fig. 2. Amplitude of the various terms in Eqs. (22)–(36) describing the focal plane angle distribution on the sky for a mock but realistic *Planck* scanning coverage (HEALPix maps at *nside* = 1024, Galactic coordinates). *From top to bottom*: $|\langle\cos 2\psi\rangle|$, $|\langle\sin 2\psi\rangle|$, $|\langle\sin 4\psi\rangle|/2$, $\langle\cos^2 2\psi\rangle$.

6.2. Results for E and B-mode power spectra

The semi-analytical method described in Sect. 5 is able to propagate instrumental errors up to the six CMB power spectra: TT, EE, BB, TE, TB and EB. In this section, we will focus on the E and B-mode power spectra and discuss results obtained for *Planck*-HFI in case of absolute (Sect. 6.2.1) and relative uncertainties (Sect. 6.2.2). Other spectra (like TB and EB) that are predicted to be null for CMB signal, can be very useful in revealing "leakage" due to systematics. However, many systematic effects can produce such leakage, which will make their separate identification very complicated when using only these modes.

6.2.1. Global error over the focal plane/calibration on the sky

Absolute calibration of total power is done using the orbital dipole that has the same electromagnetic spectrum as the CMB and is not degenerate with the underlying sky signal as its sign changes after 6 months of observation. From Eqs. (23) and (24), absolute error on the gain g will not produce any leakage in polarization signals:

$$\Delta^{g}\boldsymbol{s} = \begin{pmatrix} \gamma & 0 & 0 \\ 0 & 0 & 0 \\ 0 & 0 & 0 \end{pmatrix}\boldsymbol{s} \quad \text{for gain.} \quad (37)$$

As far as polarization is concerned, we need a polarized source on the sky. The Crab nebulae, a supernova remnant, is a good candidate as it shows a large polarization emission in the *Planck*-HFI frequency bands. It has been observed in a wide range

of frequencies and shown to have polarization properties stable enough to be a calibrator for polarization experiments. Dedicated observations of this source were done by IRAM at 89 GHz (Aumont et al. 2010). The impact of an approximate knowledge of the polarization sky calibrator leads to a uniform error over the focal plane. In this case, the ω and ϵ parameters do not depend on the detector. From Eqs. (25)–(36), we found that the intensity does not leak into polarization with polarization efficiency and orientation errors ($\Delta_{IQ} = \Delta_{IU} = 0$) and

$$\Delta^{\rho}\boldsymbol{s} = \begin{pmatrix} 0 & 0 & 0 \\ 0 & \epsilon & 0 \\ 0 & 0 & \epsilon \end{pmatrix} \boldsymbol{s} \quad \text{for polarization efficiency,} \tag{38}$$

$$\Delta^{\alpha}\boldsymbol{s} = \begin{pmatrix} 0 & 0 & 0 \\ 0 & \cos 2\omega & \sin 2\omega \\ 0 & -\sin 2\omega & \cos 2\omega \end{pmatrix} \boldsymbol{s} \quad \text{for orientation.} \tag{39}$$

In terms of power spectra, an error in polarization efficiencies only affects the amplitude of the E and B power spectra but does not result in leakage from E to B. On the other hand, an error in orientations mixes Q and U maps resulting in both a leakage from E into B (as well as B into E) and a modification of E and B amplitudes. However, as the E-mode signal is far above that of the B-mode in amplitude, ΔC_ℓ is dominated by E-mode to second order:

$$\Delta C_\ell^X = 2\epsilon C_\ell^X + 4\omega^2 C_\ell^E, \tag{40}$$

for X either E or B-mode.

Consequently, for E-mode, the polarization efficiency uncertainty must be $\epsilon < 0.5\%$ and the orientation uncertainty $\omega < 2\overset{\circ}{.}9$ to obtain less than 1% error on the power spectrum amplitude. Alternatively, the leakage is kept under 10% of the cosmic variance if $\epsilon < 0.3\%$ and $\omega < 2\overset{\circ}{.}1$ for $\ell = 2{-}1000$.

To go further and target the B-mode signal, we show that the orientation must be known to better than $1\overset{\circ}{.}3$ ($0\overset{\circ}{.}4$) in order to keep the leakage from E to B-mode lower than 10% (1%) of the expected C_ℓ^B for a tensor-to-scalar ratio of $r = 0.05$ at large angular scales ($\ell < 100$). The error on its amplitude will be driven by the polarization efficiency uncertainty (2ϵ).

6.2.2. Relative calibration between detectors

As discussed in Sect. 6.1, there is no generic case concerning the a priori distribution of errors for polarization parameters on HFI. We therefore performed 10 000 Monte-Carlo simulations to propagate the errors through to the E and B polarized angular power spectra. Errors were drawn from a gaussian distribution with various dispersions σ_γ, σ_ϵ and σ_ω per detector. We then propagated those uncertainties through to the E and B angular power spectra.

The results show leakage coming from TT, EE and BB depending on the parameter considered. The gain uncertainty induces leakage from intensity into polarization so ΔC_ℓ show leakage from TT and TE spectra (dominated by TT). For polarization efficiency and orientation, ΔC_ℓ is a combination of EE and BB power spectra with relative weights that depend on the distribution of uncertainties between the four bolometers considered. Due to second order terms, the distribution of errors in the angular power spectra is highly non gaussian, as shown in Figs. 3–5.

We then compare the rms of those distributions for each multipole to the cosmic variance of the E-mode and to an $r = 0.05$ B-mode spectrum with lensing (Figs. 6–8).

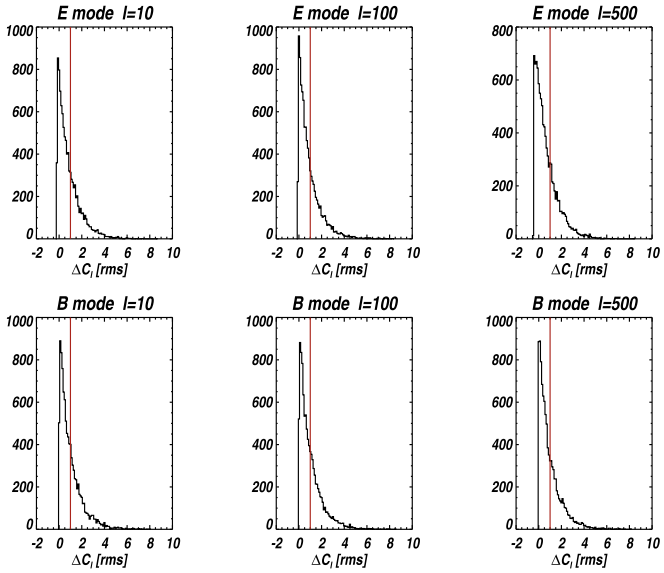

Fig. 3. Distribution of ΔC_ℓ^{EE} (*top*) and ΔC_ℓ^{BB} (*bottom*) for $\sigma_\gamma = 0.2\%$ gain errors for multipoles $\ell = 10$, $\ell = 100$, $\ell = 500$, normalized to their rms (*red line*).

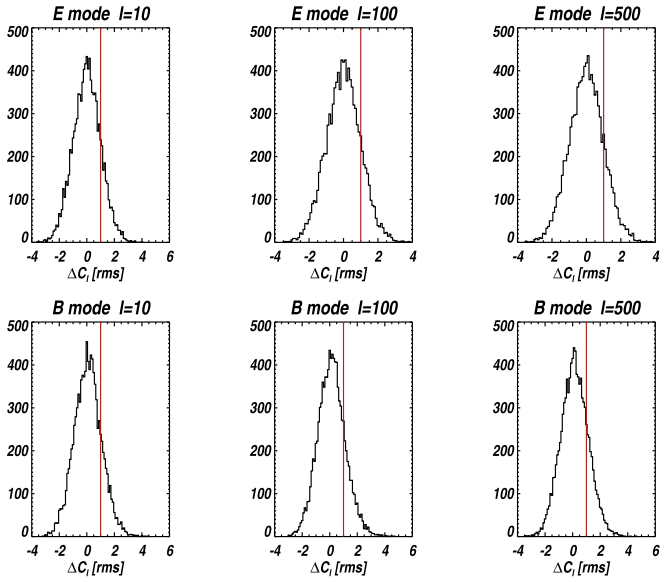

Fig. 4. Distribution of ΔC_ℓ^{EE} (*top*) and ΔC_ℓ^{BB} (*bottom*) for $\sigma_\epsilon = 1\%$ polar efficiency errors for multipoles $\ell = 10$, $\ell = 100$, $\ell = 500$, normalized to their rms (*red line*).

Using these results, we can set the requirements for *Planck*-HFI on the calibration of gain, polarization efficiency and orientation. More precisely, we demand that the errors on the temperature and polarization calibration parameters to be such that the induced leakage into the E power spectrum is lower than 10% of the cosmic variance over the multipole range $\ell = 2{-}1000$. This means that gains must be known to 0.15%, polarization efficiencies to 0.5% and detector orientations to 1°.

According to Efstathiou & Gratton (2009), an extended *Planck* mission should be able to measure gravitational B-mode at a level of $r = 0.05$ and put an upper-limit of $r = 0.03$ when considering foreground residuals and noise levels. To achieve such a detection (or upper-limit), the constraints on the calibration parameters must be much tighter. For this goal, we set the leakage into B power spectrum to be 10% of the B-mode model

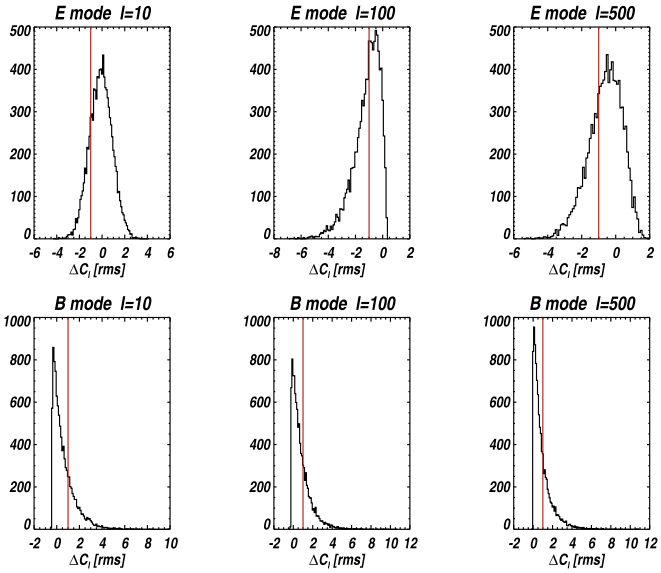

Fig. 5. Distribution of ΔC_ℓ^{EE} (*top*) and ΔC_ℓ^{BB} (*bottom*) for $\sigma_\omega = 1°$ orientation errors for multipoles $\ell = 10$, $\ell = 100$, $\ell = 500$, normalized to their rms (*red line*).

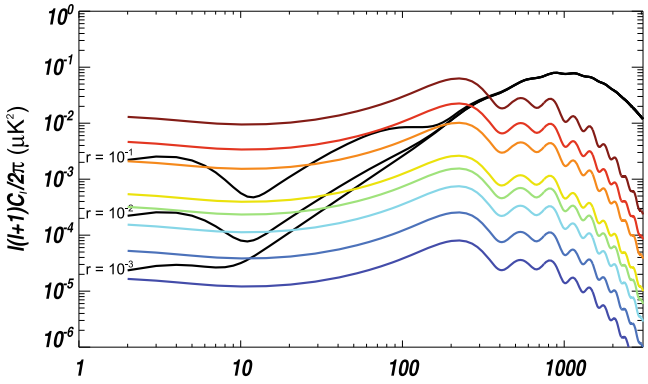

Fig. 6. ΔC_ℓ in rms due to gain errors from 0.01% to 1% for *E*-mode (*top*) and *B*-mode (*bottom*) compared to initial spectrum (*solid black lines*). Cosmic variance for *E*-mode is plotted in *dashed black line*.

we want to target, for a multipole range from $\ell = 2$ to 100. With such an hypothesis, we find that the gain precision should be better than 0.05% and the orientations of the bolometers should be known to better than 0.°75. The leakage due to polarization efficiency into *B*-mode is very small (see bottom plot in Fig. 7), thus the constraint on the polarization efficiency determination is not relevant in that case (we found 10%).

7. Ground measurements

The *Planck*-HFI polarization calibration on ground was divided into two parts: polarization efficiencies were measured for each detector separately, before focal plane assembly, at the University of Wales in Cardiff in 2005, while orientations of the PSBs with respect to the focal plane were measured during the overall calibration of the *Planck* HFI in the Saturne cryostat at Orsay, France, in 2006.

7.1. Polarization efficiency ground measurements

Detector-level polarization efficiency measurements were performed in a 2-stage adiabatic demagnetization refrigerator

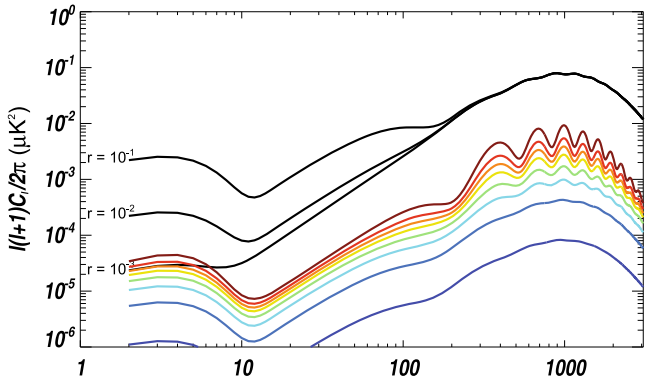

Fig. 7. ΔC_ℓ in rms due to polarization efficiency errors from 0.1% to 4% for *E*-mode (*top*) and *B*-mode (*bottom*) compared to initial spectrum (*solid black lines*). Cosmic variance for *E*-mode is plotted in *dashed black line*.

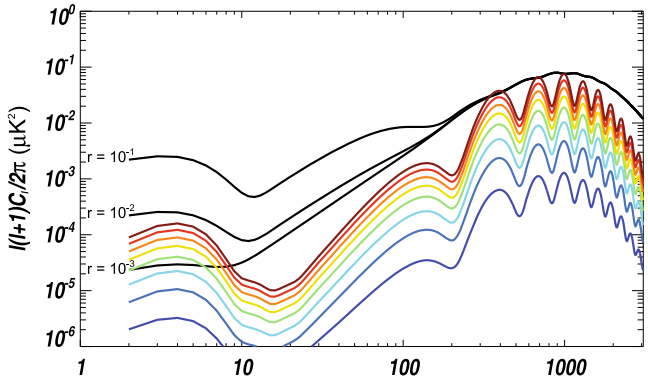

Fig. 8. ΔC_ℓ in rms due to various orientation errors from 0.25 to 2 degrees for *E*-mode (*top*) and *B*-mode (*bottom*) compared to initial spectrum (*solid black lines*). Cosmic variance for *E*-mode is plotted in *dashed black line*.

(ADR) at a base temperature of 200 mK. The ADR was configured to take six detectors per cooldown (in most cases all of the same optical band per cooldown). Thermal blocking filters were used at the 4 K, 77 K and 300 K stages of the testbed. The anti-reflective coating on the cryostat window was matched to the optical band under test. The window, of 125 mm diameter, and all the thermal blockers were sized such that they filled the beams. The polarization source was a rotating polarizer grid positioned over an extended temperature-controlled black body source of 75 mm diameter running at 126°C. The final source aperture was 70 mm in diameter. The mechanical structure of the source was fully clad with non-rotating Eccosorb (type AN-72). The source was positioned approximately 690 mm from the cryostat window, tilted 4.°8 off the optical axis, and mechanically chopped at 6 Hz. The experimental setup was fully surrounded with Eccosorb (type AN-72) while the data were recorded. Data were recorded in a step and sample fashion over five full rotations of the polarizer grid with a 4° step size and a 4 s integration time.

Detailed results are given in the appendix in Tables B.1 and B.2 for PSBs and SWBs, respectively. The polarization efficiency of the SWBs is low, as expected, and range between 1.6% and 8.6%. The statistical error is typically 0.5%, and as much as 1.8% for one SWB. The polarization efficiency of the PSBs is typically around 90%, ranging from 84% to 96%, with errors below 0.3%.

7.2. Orientation ground measurements

7.2.1. The calibration setup

The orientation calibration was performed within a 1-m diameter cryostat cooled to 2 K, to be close to flight conditions (for a more detailed description of the calibration setup and photographs, see Pajot et al. 2010). The detectors were cooled to their nominal operating temperature, 100 mK. For polarization measurements, the source (Cold Source 2 or CS2) was a blackbody at 20 K whose radiation was diluted within a 50 cm diameter sphere in order to illuminate, after a reflection from mirror, the full focal plane at once. The source was modulated by a diapason at a fixed frequency of 10 Hz. The radiation was linearly polarized by an aluminum grid deposited on a 138 mm diameter mylar film. The aluminum strips of the polarizer were 5 μm wide, 5 μm thick and spaced 5 μm apart. The Mylar film itself was 10 μm thick, with a transmission coefficient greater than 0.9; the polarization efficiency of the polarizer was measured to be better than 99.9%, so it can be assumed equal to unity at HFI frequencies. The polarizer could rotate freely around its axis using a stepper motor. There are exactly 32 000 steps in one rotation, so the precision in relative angle is better than 1′.

7.2.2. Reference for angle measurement

The reference position was defined by a pin fixed to the polarizer, which was detected by electric contact with a copper strip with a precision of ±5 motor steps, i.e. ±0.°06. We measured the angle of this reference position with respect to the focal plane using the light of a laser diffracted by the strips of the polarizer; the diffraction pattern is formed by points aligned orthogonally to the strips (i.e. parallel to the transmitted polarization).

Two different methods were used to determine polarization angles with respect to the focal plane. In the first method, we measured the orientation with respect to the platform and used the mechanical position of the instrument with respect to the platform to get the absolute angle. In the second method, we measured the angle directly with respect to the instrument. In both cases, we measured the same angle and checked it was constant across the polarizer. Both methods gave similar error estimates on the reference position angle, which can safely be assumed to be lower than 0.°3:

$$\left|\Delta\theta^{\text{absolute}}\right| < 0.^{\circ}3. \tag{41}$$

7.2.3. Data analysis

For this measurement, the polarizer was rotated by 5° steps and signal was inegrated for 20 s at each position. Eight full rotations of the polarizer were performed.

At each polarizer position, the signal from the source is sinusoidal with a frequency of 10 Hz. It is demodulated fitting a sine curve over a few periods, yielding around 60 independent measurements for each stationary period of 20 s. The average and standard deviation of these 60 measurements give the signal and its error for each 20 s period, for a fixed position of the polarizer. The statistical error was found to be typically below 1% of the signal.

We then fit the signal as a function of the polarizer angle to estimate the polarization efficiency and the orientation of the detectors. However, despite the good quality of the polarizer, we found cross-polarization leakage of around 30%, much higher than that found in Sect. 7.1, with the Cardiff measurements: it was probably due to standing waves between the polarizer and the focal plane and made the detector polarization efficiency unmeasurable with this setup. The angle that maximizes the signal gives the orientation of the polarizer; however, the PSB angle must be given in the horn aperture plane, which is slightly out of parallel with the polarizer plane. We have performed ray-tracing simulations to estimate and correct for this geometrical effect. The corrections lie between −0.°5 to 0.°5, and the precision (set by the precision on the position of the polarizer) is better than 0.°15.

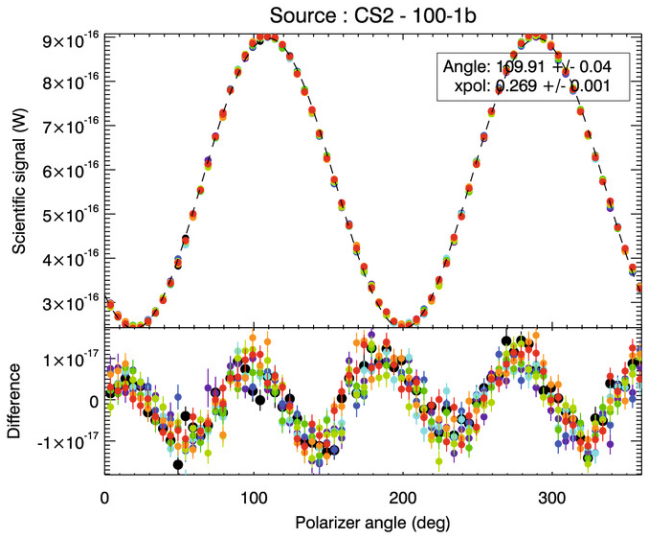

Fig. 9. Signal of PSB 100-1b with respect to the angle in the horn aperture plane; each color represents one rotation of the polarizer (8 turns); the signal is fitted using a standard sine curve. The difference exhibits a systematic effect that can be explained by standing waves between the polarizer and the focal plane (see text).

Figure 9 shows the curve obtained for a PSB at 100 GHz and the difference with the fitted model. The residuals show a 90°-periodic sine curve, which is present in some detectors. Some detectors also have glitches, reproduced at the same position at each rotation of the polarizer. These glitches mostly affect the highest two frequency channels (545 and 857 GHz), i.e., only SWBs. As $\cos 2\theta$ and $\cos 4\theta$ are orthogonal functions over 2π, the fitted values for the angle and the polarization efficiency are unchanged when adding such a term in the fitting model. However, we cannot exclude that they may be contaminated by a systematic effect like some other modes (mainly in mode $\cos 4\theta$). For example, if the incoming radiation is the sum of two partially linearly polarized radiations, one with orientation θ (rotating with the polarizer) and one with fixed orientation θ_0, the signal measured by the detector reads:

$$\begin{aligned} s(\theta) \propto\ & 1 + \rho \cos 2(\theta - \theta_{\text{det}}) \\ & + \rho' \cos 2(\theta - \theta_0)\,[1 - \cos 2(\theta - \theta_{\text{det}})] \end{aligned} \tag{42}$$

where θ_{det} is the polarization orientation of the detector. In this model, the angle measured through the phase of the mode $\cos 2\theta$ will not be the detector polarization angle.

More generally, we can expand the signal as a Fourier series $s(\theta) = \sum_{n=-N}^{+N} c_n e^{in\theta}$ and fit its coefficients c_n (which fulfill the condition $c_{-n}^{\star} = c_n$, as s is a real quantity). The coefficient c_2, giving the dependence in $\cos 2\theta$, contains the information on polarization efficiency and angle through its modulus and argument, and is independent of the other modes. To estimate the error on the polarization angle without relying on a particular model, we assume that the mode c_2 is the sum of two contributions, $c_2 = c_2^{\text{pol}} + c_2^{\text{syst}}$ (true polarization signal and induced

systematic effect). The maximum systematic error on the angle is then given by:

$$\max\left|\Delta\theta^{\rm syst}\right| = \arctan\left|\frac{c_2^{\rm syst}}{c_2^{\rm pol}}\right|. \quad (43)$$

We draw an upper bound on the systematic error by assuming that $|c_2^{\rm syst}/c_2^{\rm pol}| \lesssim \max_{n\neq 0,2}|c_n/c_2|$. However, as the systematic error is due to complex interference between the polarizer, the focal plane and the horns, we chose a conservative limit by taking for all detectors the maximum of this estimate among all PSBs. The statistical error on the coefficients c_n being negligible compared to the systematic error, we finally find the following upper limit on the total error on the relative angle of each polarization sensitive detectors:

$$\left|\Delta\theta^{\rm relative}\right| < 0.^\circ 9. \quad (44)$$

As an independent check, we compared the relative angle between PSBs within each horn (which is close but not exactly equal to 90°) with the angles found using the setup described in Sect. 7.1. We found an agreement within the systematic error bars for all horns except one, which is, however, within the statistical plus systematic error bar (the statistical error coming from the Cardiff measurements).

The case of SWBs is treated separately, as the statistical error is not negligible in this case (due to the low polarization efficiencies). We performed a similar analysis, taking into account the statistical error. The results are gathered in Table B.2. Note that the SWBs are not meant to be used for polarization measurements.

8. Discussion and conclusion

This paper focuses on the impact of polarized calibration parameters (gain, polarization efficiency and detector orientation) on power spectra in the context of *Planck*-HFI. We have developed a semi-analytical method that allows us to compute quickly and easily the impact of uncertainties on gain, polarization efficiency and orientation on the E and B-mode power spectra, while exactly accounting for the scanning strategy and the combination of different detectors. We used this method in the particular case of *Planck*-HFI and derived constraints on the gain, polarization efficiency and detector orientation needed to achieve *Planck*-HFI's scientific goals.

Planck will use the orbital dipole to calibrate the total power for each detector. We find that the relative uncertainty on the gain must be lower than 0.15% to keep systematic error on E-mode power spectrum below 10% of the cosmic variance in the multipole range $\ell = 2{-}1000$. Given the 0.2% accuracy on relative gain obtained by WMAP (Hinshaw et al. 2009), we expect that HFI can achieve the 0.15% requirements, thanks to the higher gain stability expected for HFI.

We show that the polarization efficiency uncertainty must be below 0.3% in order to achieve the required sensitivity for the E-mode. The error on the primordial B-mode power spectrum will be kept below 10% of the signal expected from a tensor-to-scalar ratio $r = 0.05$ in the multipole range $\ell = 2{-}100$ if the polarization efficiency is known to better than 10.3%. In this paper, we have presented the results of the ground measurements on HFI PSBs polarization efficiency, which show an accuracy of 0.3% that fulfills the requirements for both E and B-modes.

For the polarization orientation, we have distinguished a global orientation error of the focal plane (which affects identically all detectors) from a relative error (different for each detector). For E-modes, we show that the requirement is $2.^\circ 1$ on the global orientation knowledge and 1° on the relative orientation to keep the error below 10% of the cosmic variance in the range $\ell = 2{-}1000$. Both these requirements are already fulfilled by the ground measurements, in which we found $0.^\circ 3$ and $0.^\circ 9$ respectively. In order to measure a B-mode signal with a systematic error lower than 10% for a tensor-to-scalar ratio $r = 0.05$, the global orientation must be known to better than $1.^\circ 2$ and the relative orientation at better than $0.^\circ 75$. While the ground measurements fulfill the requirement on global orientation, the relative orientation knowledge will need to be improved in flight. For *Planck*, we plan to use the Crab nebula as the primary polarization calibrator (Aumont et al. 2010), which will also allow the results presented in this paper to be cross-checked. The accuracy of the ground measurements of polarization efficiencies and orientations will allow the E-mode power spectrum to be measured, with systematic errors lower than 10% of the cosmic variance, provided that the other sources of systematic effects are controlled.

Acknowledgements. The *Planck*-HFI instrument (http://hfi.planck.fr/) was designed and built by an international consortium of laboratories, universities and institutes, with important contributions from the industry, under the leadership of the PI institute, IAS at Orsay, France. It was funded in particular by CNES, CNRS, NASA, STFC and ASI. The authors extend their gratitude to the numerous engineers and scientists, who have contributed to the design, development, construction or evaluation of the HFI instrument. The authors are pleased to thank the referee for his/her very useful remarks.

References

Aumont, A., Conversi, L., Falgarone, E., et al. 2010, A&A, 514, A70
Bock, J. J., Chen, D., & Mauskopf, P. D. 1995, Space Sci. Rev., 74, 229
Born, M., & Wolf, E. 1964, Principles of Optics (Pergamon Press)
Couchot, F., Delabrouille, J., Kaplan, J., & Revenu, B. 1999, A&AS, 135, 579
Ditchburn, R. W. 1976, Light, vol. I (Academic Press)
Dunkley, J., Komatsu, E., Nolta, M. R., et al. 2009, ApJS, 180, 306
Efstathiou, G., & Gratton, S. 2009, J. Cosmol. Astro-Part. Phys., 6, 11
Fixsen, D. J., Cheng, E. S., Cottingham, D. A., et al. 1994, ApJ, 420, 445
Górski, K. M., Hivon, E., Banday, A. J., et al. 2005, ApJ, 622, 759
Grain, J., Tristram, M., & Stompor, R. 2009, Phys. Rev. D, 79, 123515
Hinshaw, G., Weiland, J. L., Hill, R. S., et al. 2009, ApJS, 180, 225
Hu, W., Hedman, M. M., & Zaldarriaga, M. 2003, Phys. Rev. D, 67, 043004
Jones, R. C. 1941, J. Opt. Soc. Am., 31, 488
Jones, W. C., Bhatia, R. S., Bock, J. J., & Lange, A. E. 2003, in SPIE Proc., 4855, 227
Kogut, A., Spergel, D. N., Barnes, C., et al. 2003, ApJS, 148, 161
Komatsu, E., Dunkley, J., Nolta, M. R., et al. 2009, ApJS, 180, 330
Kovac, J., Leitch, E. M., Pryke, C., et al. 2002, Nature, 420, 772
Lamarre, J.-M., Puget, J.-L., Ade, P. A. R., et al. 2010, A&A, 520, A9
Leahy, J. P., Bersanelli, M., D'Arcangelo, O., et al. 2010, A&A, 520, A8
Lewis, A., Challinor, A., & Turok, N. 2002, Phys. Rev. D, 65, 023505
Maffei, B., Noviello, F., Murphy, J. A., et al. 2010, A&A, 520, A12
Montroy, T., Ade, P. A. R., Bock, J. J., et al. 2006, ApJ, 647, 813
O'Dea, D., Challinor, A., & Johnson, B. R. 2007, MNRAS, 376, 1767
Page, L., Hinshaw, G., Komatsu, E., et al. 2007, ApJS, 170, 335
Pajot, F., Ade, P. A. R., Beney, J.-L., et al. 2010, A&A, 520, A10
QUaD collaboration: Pryke, C., Ade, P., Bock, J., et al. 2009, ApJ, 692, 1247
Readhead, A. C. S., Myers, S. T., Pearson, T. J., et al. 2004, Science, 306, 836
Rosset, C., Yurchenko, V., Delabrouille, J., et al. 2007, A&A, 464, 405
Shimon, M., Keating, B., Ponthieu, N., & Hivon, E. 2008, Phys. Rev. D, 77, 083003
Tauber, J. A., Noigaard-Nielsen, H. U., Ade, P. A. R., et al. 2010a, A&A, 520, A2
Tauber, J. A., Mandolesi, N., Pujet, J.-L., et al. 2010b, A&A, 520, A1
Tristram, M., Macias-Perez, J., Renault, C., & Santos, D. 2005, MNRAS, 358, 833
Wu, J. H. P., Zuntz, J., Abroe, M. E., et al. 2007, ApJ., 665, 55
Yun, M., Bock, J. J., Holmes, W., Koch, T., & Lange, A. E. 2004, J. Vac. Sci. Technol. B, 22, 220
Zaldarriaga, M., & Seljak, U. 1997, Phys. Rev. D, 55, 1830

Appendix A: Explicit forms of pointing related functions

We write the projection of the signal $\boldsymbol{m}$ into a sky map $\boldsymbol{s}$ as

$$\hat{\boldsymbol{s}} = (\tilde{A}^T\tilde{A})^{-1}\tilde{A}^T\boldsymbol{m} \tag{A.1}$$

$$= \left[\sum_d \tilde{A}_d^T\tilde{A}_d\right]^{-1}\left[\sum_d \tilde{A}_d^T A_d\boldsymbol{s}\right] \tag{A.2}$$

$$= \left[\sum_d \tilde{A}_d^T\tilde{A}_d\right]^{-1}\left[\sum_d \Lambda_d(\gamma_d,\epsilon_d,\omega_d)\boldsymbol{s}\right]. \tag{A.3}$$

Where A is the pointing matrix. In this expression, $\Lambda_d(\gamma_d,\epsilon_d,\omega_d)$ is an explicit function of γ_d, ϵ_d and ω_d. $\tilde{g}$, $\tilde{\rho}$ and $\tilde{\alpha}$ are only parameters. If we note $t(d)$ the data samples of detector d, Λ_d reads

$$\Lambda_d = \sum_{t(d)}\begin{pmatrix} (1+\gamma) & (\tilde{\rho}_d+\epsilon_\rho)\cos 2(\tilde{\psi}_d(t)+\omega_d) & (\tilde{\rho}_d+\epsilon_\rho)\sin 2(\tilde{\psi}_d(t)+\omega_d) \\ (1+\gamma)\tilde{\rho_d}\cos 2\tilde{\psi}_d(t) & \tilde{\rho_d}(\tilde{\rho}_d+\epsilon_\rho)\cos 2\tilde{\psi}_d(t)\cos 2(\tilde{\psi}_d(t)+\omega_d) & \tilde{\rho_d}(\tilde{\rho}_d+\epsilon_\rho)\cos 2\tilde{\psi}_d(t)\sin 2(\tilde{\psi}_d(t)+\omega_d) \\ (1+\gamma)\tilde{\rho_d}\sin 2\tilde{\psi}_d(t) & \tilde{\rho_d}(\tilde{\rho}_d+\epsilon_\rho)\sin 2\tilde{\psi}_d(t)\cos 2(\tilde{\psi}_d(t)+\omega_d) & \tilde{\rho_d}(\tilde{\rho}_d+\epsilon_\rho)\sin 2\tilde{\psi}_d(t)\sin 2(\tilde{\psi}_d(t)+\omega_d) \end{pmatrix}. \tag{A.4}$$

Considering small variations around $\tilde{g}$, $\tilde{\rho}$ and $\tilde{\alpha}$, we can write the perturbative expansion to first order for both $\gamma \ll 1$, $\epsilon \ll 1$ and $\omega \ll 1$:

$$\Delta\boldsymbol{s} = \hat{\boldsymbol{s}} - \boldsymbol{s} \tag{A.5}$$

$$= \left[\sum_d \tilde{A}_d^T\tilde{A}_d\right]^{-1}\left[\sum_d \tilde{A}_d^T A_d - \tilde{A}_d^T\tilde{A}_d\right]\boldsymbol{s}$$

$$\equiv \left[\sum_d \tilde{A}_d^T\tilde{A}_d\right]^{-1}\left[\sum_d \Lambda_d(\gamma_d,\epsilon_d,\omega_d) - \Lambda_d(0,0,0)\right]\boldsymbol{s}$$

$$\simeq \left[\sum_d \tilde{A}_d^T\tilde{A}_d\right]^{-1}\sum_d\left[\frac{\partial\Lambda_d}{\partial\gamma_d}\gamma_d + \frac{\partial\Lambda_d}{\partial\epsilon_d}\epsilon_d + \frac{\partial\Lambda_d}{\partial\omega_d}\omega_d\right]\boldsymbol{s}. \tag{A.6}$$

Straightforward generalization to second order reads:

$$\Delta\boldsymbol{s} = \left[\sum_d \tilde{A}_d^T\tilde{A}_d\right]^{-1}\sum_d\left[\sum_{e\in\{\gamma,\epsilon,\omega\}}\frac{\partial\Lambda_d}{\partial e_d}e_d + \frac{1}{2}\sum_{(e,e')\in\{\gamma,\epsilon,\omega\}}\frac{\partial^2\Lambda_d}{\partial e_d\partial e'_d}e_d e'_d\right]\boldsymbol{s}. \tag{A.7}$$

Derivatives of $\Lambda_d(\gamma_d,\epsilon_d,\omega_d)$ with respect to uncertainties of gain γ, polarization efficiency ϵ and detector orientation ω are given by

$$\left.\frac{\partial\Lambda_d}{\partial\gamma_d}\right|_{(0,0,0)} = \sum_{t(d)}\begin{pmatrix} 1 & 00 \\ \cos 2\tilde{\psi}_d(t) & 00 \\ \sin 2\tilde{\psi}_d(t) & 00 \end{pmatrix} \tag{A.8}$$

$$\left.\frac{\partial\Lambda_d}{\partial\epsilon_d}\right|_{(0,0,0)} = \sum_{t(d)}\begin{pmatrix} 0 & \cos 2\tilde{\psi}_d(t) & \sin 2\tilde{\psi}_d(t) \\ 0 & \tilde{\rho_d}\cos^2 2\tilde{\psi}_d(t) & \tilde{\rho_d}\cos 2\tilde{\psi}_d(t)\sin 2\tilde{\psi}_d(t) \\ 0 & \tilde{\rho_d}\cos 2\tilde{\psi}_d(t)\sin 2\tilde{\psi}_d(t) & \tilde{\rho_d}\sin^2 2\tilde{\psi}_d(t) \end{pmatrix} \tag{A.9}$$

$$\left.\frac{\partial\Lambda_d}{\partial\omega_d}\right|_{(0,0,0)} = \sum_{t(d)}\begin{pmatrix} 0 & -2\tilde{\rho_d}\sin 2\tilde{\psi}_d(t) & 2\tilde{\rho_d}\cos 2\tilde{\psi}_d(t) \\ 0 & -2\tilde{\rho_d}^2\cos 2\tilde{\psi}_d(t)\sin 2\tilde{\psi}_d(t) & 2\tilde{\rho_d}^2\cos^2 2\tilde{\psi}_d(t) \\ 0 & -2\tilde{\rho_d}^2\sin^2 2\tilde{\psi}_d(t) & 2\tilde{\rho_d}^2\cos 2\tilde{\psi}_d(t)\sin 2\tilde{\psi}_d(t) \end{pmatrix}. \tag{A.10}$$

And second order derivatives reads

$$\left.\frac{\partial^2\Lambda_d}{\partial\gamma_d^2}\right|_{(0,0,0)} = 0 \tag{A.11}$$

$$\left.\frac{\partial^2\Lambda_d}{\partial\epsilon_d^2}\right|_{(0,0,0)} = 0 \tag{A.12}$$

$$\left.\frac{\partial^2\Lambda_d}{\partial\omega_d^2}\right|_{(0,0,0)} = \sum_{t(d)}\begin{pmatrix} 0 & -4\tilde{\rho_d}\cos 2\tilde{\psi}_d(t) & -4\tilde{\rho_d}\sin 2\tilde{\psi}_d(t) \\ 0 & -4\tilde{\rho_d}^2\cos^2 2\tilde{\psi}_d(t) & -4\tilde{\rho_d}^2\cos 2\tilde{\psi}_d(t)\sin 2\tilde{\psi}_d(t) \\ 0 & -4\tilde{\rho_d}^2\cos 2\tilde{\psi}_d(t)\sin 2\tilde{\psi}_d(t) & -4\tilde{\rho_d}^2\sin^2 2\tilde{\psi}_d(t) \end{pmatrix} \tag{A.13}$$

$$\left.\frac{\partial^2\Lambda_d}{\partial\epsilon_d\partial\omega_d}\right|_{(0,0,0)} = \sum_{t(d)}\begin{pmatrix} 0 & -2\sin 2\tilde{\psi}_d(t) & 2\cos 2\tilde{\psi}_d(t) \\ 0 & -4\tilde{\rho_d}\cos 2\tilde{\psi}_d(t)\sin 2\tilde{\psi}_d(t) & 4\tilde{\rho_d}\cos^2 2\tilde{\psi}_d(t) \\ 0 & -4\tilde{\rho_d}\sin^2 2\tilde{\psi}_d(t) & 4\tilde{\rho_d}\cos 2\tilde{\psi}_d(t)\sin 2\tilde{\psi}_d(t) \end{pmatrix} \tag{A.14}$$

$$\left.\frac{\partial^2\Lambda_d}{\partial\gamma_d\partial\epsilon_d}\right|_{(0,0,0)} = \left.\frac{\partial^2\Lambda_d}{\partial\gamma_d\partial\omega_d}\right|_{(0,0,0)} = 0. \tag{A.15}$$

Appendix B: Polarization efficiencies and angles

Table B.1. Polarization efficiencies and orientations for *Planck*-HFI PSBs.

Bolometer (PSB)	Polarization efficiency [%]	Polarization angle
100-1a	94.7 ± 0.2	*21.°1 ± 0.°9 [rel] ± 0.°3 [abs]
100-1b	94.3 ± 0.3	109.°9 ± 0.°9 [rel] ± 0.°3 [abs]
100-2a	96.2 ± 0.2	*44.°3 ± 0.°9 [rel] ± 0.°3 [abs]
100-2b	90.2 ± 0.2	133.°5 ± 0.°9 [rel] ± 0.°3 [abs]
100-3a	90.1 ± 0.3	**0.°7 ± 0.°9 [rel] ± 0.°3 [abs]
100-3b	93.4 ± 0.2	*90.°6 ± 0.°9 [rel] ± 0.°3 [abs]
100-4a	95.7 ± 0.3	158.°5 ± 0.°9 [rel] ± 0.°3 [abs]
100-4b	92.3 ± 0.2	*70.°0 ± 0.°9 [rel] ± 0.°3 [abs]
143-1a	83.3 ± 0.2	*42.°9 ± 0.°9 [rel] ± 0.°3 [abs]
143-1b	84.6 ± 0.2	135.°2 ± 0.°9 [rel] ± 0.°3 [abs]
143-2a	87.5 ± 0.3	*44.°2 ± 0.°9 [rel] ± 0.°3 [abs]
143-2b	89.3 ± 0.3	134.°0 ± 0.°9 [rel] ± 0.°3 [abs]
143-3a	83.9 ± 0.2	**0.°4 ± 0.°9 [rel] ± 0.°3 [abs]
143-3b	89.9 ± 0.2	*93.°7 ± 0.°9 [rel] ± 0.°3 [abs]
143-4a	93.1 ± 0.2	**3.°1 ± 0.°9 [rel] ± 0.°3 [abs]
143-4b	92.8 ± 0.2	*91.°5 ± 0.°9 [rel] ± 0.°3 [abs]
217-5a	95.0 ± 0.1	*44.°7 ± 0.°9 [rel] ± 0.°3 [abs]
217-5b	95.2 ± 0.2	133.°9 ± 0.°9 [rel] ± 0.°3 [abs]
217-6a	94.9 ± 0.2	*45.°0 ± 0.°9 [rel] ± 0.°3 [abs]
217-6b	95.4 ± 0.2	134.°8 ± 0.°9 [rel] ± 0.°3 [abs]
217-7a	94.0 ± 0.2	**0.°3 ± 0.°9 [rel] ± 0.°3 [abs]
217-7b	93.7 ± 0.1	*91.°2 ± 0.°9 [rel] ± 0.°3 [abs]
217-8a	94.2 ± 0.1	**2.°2 ± 0.°9 [rel] ± 0.°3 [abs]
217-8b	94.1 ± 0.1	*92.°5 ± 0.°9 [rel] ± 0.°3 [abs]
353-3a	88.7 ± 0.1	*44.°1 ± 0.°9 [rel] ± 0.°3 [abs]
353-3b	92.0 ± 0.1	132.°4 ± 0.°9 [rel] ± 0.°3 [abs]
353-4a	87.0 ± 0.1	*45.°3 ± 0.°9 [rel] ± 0.°3 [abs]
353-4b	91.4 ± 0.1	135.°2 ± 0.°9 [rel] ± 0.°3 [abs]
353-5a	84.4 ± 0.1	178.°4 ± 0.°9 [rel] ± 0.°3 [abs]
353-5b	87.4 ± 0.1	*90.°3 ± 0.°9 [rel] ± 0.°3 [abs]
353-6a	87.3 ± 0.1	**1.°3 ± 0.°9 [rel] ± 0.°3 [abs]
353-6b	88.5 ± 0.1	*91.°2 ± 0.°9 [rel] ± 0.°3 [abs]

Notes. Ideal PSBs should have a 100% polarization efficiency. The error on polarization efficiency is only statistical. Error on polarization orientation is due to systematics: the absolute error is due to the error on the measurement of the reference position; the relative error is due to an optical systematic effect in the Saturne cryostat. The statistical errors are negligible and therefore not shown in this table.

Table B.2. Polarization efficiencies and orientations for *Planck*-HFI SWBs.

Bolometer (SWB)	Polarization efficiency [%]	Polarization angle
143-5	6.6 ± 0.3	*65.°7 ± 0.°1 [stat] ± *0.°6 [syst]
143-6	4.4 ± 0.3	*70.°6 ± 0.°2 [stat] ± *4.°7 [syst]
143-7	1.7 ± 0.4	102.°8 ± 0.°2 [stat] ± *1.°7 [syst]
143-8	1.6 ± 0.5	*75.°7 ± 0.°3 [stat] ± *4.°4 [syst]
217-1	4.0 ± 0.2	*98.°4 ± 2.°3 [stat] ± *5.°5 [syst]
217-2	2.1 ± 0.1	*82.°5 ± 1.°5 [stat] ± *4.°9 [syst]
217-3	4.1 ± 0.2	170.°9 ± 0.°9 [stat] ± *2.°1 [syst]
217-4	3.8 ± 0.6	120.°0 ± 1.°2 [stat] ± *2.°7 [syst]
353-1	3.4 ± 0.2	103.°1 ± 1.°2 [stat] ± *3.°6 [syst]
353-2	4.8 ± 0.1	114.°6 ± 0.°5 [stat] ± *2.°7 [syst]
353-7	8.1 ± 0.1	121.°5 ± 0.°8 [stat] ± *4.°2 [syst]
353-8	7.9 ± 0.1	133.°0 ± 0.°3 [stat] ± *1.°9 [syst]
545-1	4.7 ± 0.1	129.°1 ± 1.°0 [stat] ± *2.°4 [syst]
545-2	5.7 ± 0.1	139.°1 ± 0.°7 [stat] ± *1.°3 [syst]
545-3	5.3 ± 0.1	150.°3 ± 0.°8 [stat] ± *2.°4 [syst]
545-4	5.9 ± 0.1	145.°6 ± 0.°8 [stat] ± *1.°7 [syst]
857-1	7.8 ± 1.8	157.°3 ± 2.°1 [stat] ± *5.°1 [syst]
857-2	6.3 ± 0.1	108.°4 ± 4.°0 [stat] ± 16.°5 [syst]
857-3	8.6 ± 0.8	176.°8 ± 1.°4 [stat] ± *2.°6 [syst]
857-4	6.3 ± 0.8	161.°9 ± 2.°3 [stat] ± *6.°2 [syst]

Notes. Ideal SWBs should have a null polarization efficiency. Global uncertainty (0.°3) is common for all detector and not added.